



# Effect of process parameters on photophysical properties and barium molybdate phosphors characteristics

Maria Fernanda C. Abreu<sup>a,b,1</sup>, Fabiana V. Motta<sup>c</sup>, Renata C. Lima<sup>d</sup>, Maximo S. Li<sup>e</sup>,  
Elson Longo<sup>b</sup>, Ana Paula de A. Marques<sup>a,\*</sup>

<sup>a</sup>Departamento de Ciências Exatas e da Terra, UNIFESP, CEP 09972-270, Diadema, SP, Brazil

<sup>b</sup>LIEC, Departamento de Química, UFSCar, CEP 13565-905, São Carlos, SP, Brazil

<sup>c</sup>Departamento de Engenharia de Materiais, UFRN, CEP 59072-970, Natal, RN, Brazil

<sup>d</sup>Instituto de Química, UFU, CEP 38400-902, Uberlândia, MG, Brazil

<sup>e</sup>Instituto de Física de São Carlos, USP, CEP 13566-590, São Carlos, SP, Brazil

Received 5 August 2013; received in revised form 27 November 2013; accepted 28 November 2013

Available online 19 December 2013

## Abstract

Barium molybdate particles ( $\text{BaMoO}_4$ ) with uniform shapes have applications in various fields such as phosphors, optical fibers, scintillators, magnets and catalysts. In this study, two synthesis methods (microwave-assisted hydrothermal (MAH) and Complex Polymerization (CP)) were used to prepare  $\text{BaMoO}_4$  particles. The effect of the applied synthesis methodology and experimental parameters on the morphology, particle size, sample uniformity and optical properties of the  $\text{BaMoO}_4$  were studied. Scheelite-type single crystalline structures of  $\text{BaMoO}_4$  were identified by X-ray diffraction (XRD) as well as Raman and Fourier transform infrared spectroscopy (FTIR). Octahedral morphologies were characterized by field-emission scanning electron microscopy (FE-SEM). Photoluminescence (PL) spectra of the samples exhibited different emission properties which indicates a relationship with surface defect states (shallow and deep level defects) where interfaces populate additional levels in the band gap. Electronic order-disorder at short- and intermediate-ranges is generated by utilizing the synthesis method and can be modified by applied experimental parameters. If the particle size and morphology are controlled, deep and shallow defects can be controlled, and PL properties can be modified accordingly with the optical properties desired.

© 2014 Published by Elsevier Ltd and Techna Group S.r.l.

**Keywords:** A. Microwave processing; C. Optical properties; D. Transition metal oxides; Ceramics; Chemical syntheses

## 1. Introduction

Materials with a scheelite-type crystalline structure such as  $\text{BaMoO}_4$  (BMO) have excellent optical properties which facilitates their wide use as phosphors, laser materials and scintillation detectors [1–5]. Due to their excellent thermal and chemical stability, molybdates are considered good hosts for luminescent materials [6–8]. BMO is an important material belonging to the molybdate family which attracts attention due to its ability to produce green luminescence. BMO has

potential applications in various fields such as phosphors, optical fibers, scintillators, magnets and catalysts [6,7].

Barium molybdate can be synthesized by using different techniques; however, production with single crystalline structures and controlled morphology requires caution. The conventional solid-state reaction method is frequently used to obtain molybdate powders; this method produces materials with a large grain size and irregular morphology due to high annealing temperatures and long reaction times. In addition, the tendency for  $\text{MoO}_3$  to vaporize at high temperatures can result in non-homogeneous morphologies and compositions [9].

Various techniques have been employed to obtain materials similar to  $\text{BaMoO}_4$  and are discussed in this study: Czochralski, spontaneous crystallization, the CP method, MAH and calcination methods [10–16]. Nevertheless, some of these

\*Corresponding author. Tel.: +55 11 3319 3578; fax: +55 11 4043 6428.

E-mail addresses: [apamarques@unifesp.br](mailto:apamarques@unifesp.br),  
[apamarques@hotmail.com](mailto:apamarques@hotmail.com) (A.P.d.A. Marques).

<sup>1</sup>In memoriam.

methods have disadvantages with high synthesis temperatures and long reaction times which destroy the morphological homogeneity. In the CP method, synthesis occurs at low temperatures. The metal complex immobilization in these rigid organic polymeric networks can reduce the metal segregation and thus ensures compositional homogeneity at the molecular scale which decreases morphological and chemical heterogeneity problems [12,16].

The MAH method is promising for fabricating ideal micro- and nanometric material with appropriate morphologies. This method generally leads to a cost reduction due to low synthesis temperatures; it also promotes high yield reactions and enables large volume processing [1,2,15]. In a recent study, Luo et al. [17] reported BaMoO<sub>4</sub> nest-like nanostructures prepared under hydrothermal conditions. Particles with a controllable size and shape, high crystallinity and low agglomeration can be obtained using this synthetic route [1,2]. In addition, a variation of this technique (i.e., hydrothermal synthesis using a microwave (microwave-hydrothermal), is an attractive growth method for single crystals which provides advantages such as low synthesis temperatures and uniform rapid heating. The microwave energy accelerates the formation of well organized nanostructures.

Studies have shown that some experimental parameters, (including the use or absence of a capping reagent and the applied synthesis methodology) influenced morphologies, sizes and PL intensity of the final products. Therefore, in this study, two synthesis methods were used to obtain BaMoO<sub>4</sub> structures; (1) the successful synthesis by the CP method which favors morphological and chemical homogeneity, and (2) the MAH method which is a fast, simple and efficient soft chemical route to prepare complex oxide materials. Various complementary characterization techniques were used, including XRD, FTIR spectroscopy, Raman spectra and PL spectroscopy. FE-SEM was used to detect particles sizes and molybdate morphologies. Based on experimental results, in this study, it is proposed that the synthesis method and applied experimental parameters can modify PL properties in accordance with the optical properties desired.

## 2. Experimental

### 2.1. Materials

All chemical reagents are analytical grade and were used without further treatments: Molybdenum trioxide (MoO<sub>3</sub>) (Alfa Aesar, 99.95%), barium acetate ((CH<sub>3</sub>CO<sub>2</sub>)<sub>2</sub>Ba) (Alfa Aesar, 99%), citric acid (H<sub>3</sub>C<sub>6</sub>H<sub>5</sub>O<sub>7</sub>) (Mallinckrodt, 99%) and polyethylene glycol (HOCH<sub>2</sub>CH<sub>2</sub>OH) (Mw 200) (PEG 200) (Sigma-Aldrich, 99.9%).

### 2.2. Synthesis of barium molybdate (BaMoO<sub>4</sub>)

#### 2.2.1. Synthesis by the MAH method

Molybdenum trioxide ( $5 \times 10^{-3}$  mol L<sup>-1</sup>) was dissolved in 50 mL of distilled water with vigorous stirring. Then, (Ba(CH<sub>3</sub>CO<sub>2</sub>)<sub>2</sub>) ( $5 \times 10^{-3}$  mol L<sup>-1</sup>) was added under constant

stirring. The pH of the solution was adjusted to 12 by adding KOH. PEG 200 was added to the BMO-3 system which required a capping reagent. In reaction system 1 (BMO-1), the solid sample was collected in this phase; this sample was washed with water and ethanol and dried at 60 °C. BMO-2 and BMO-3 samples were heat treated using the MAH method. Both reaction systems were transferred into a sealed Teflon autoclave and placed in a domestic microwave (2.45 GHz, maximum power of 800 W). The BMO-2 system (without the addition of PEG) and the BMO-3 system (with the addition of PEG) were treated at 100 °C for 16 min with a heating rate fixed at 100 °C/min). The pressure in the sealed autoclave was stabilized at 2.0 atm. The autoclave was cooled to room temperature naturally, and the resulting white precipitate was collected, washed with water and ethanol and dried at 60 °C.

#### 2.2.2. Synthesis by the CP method

Molybdenum citrate was formed by MoO<sub>3</sub> dissolution in an aqueous solution of H<sub>3</sub>C<sub>6</sub>H<sub>5</sub>O<sub>7</sub> under constant stirring at 60–80 °C. After homogenization, a stoichiometric amount of Ba<sup>2+</sup> was added to the molybdenum citrate solution. The complex which formed was stirred for several hours at 60–80 °C. Then, to produce a clear and homogeneous solution, ethylene glycol was added to promote the polyesterification. With continued heating at 80–90 °C, the viscosity of the solution increased, and phase separation was not observed. The molar ratio between barium and molybdenum cations was 1:1, and the ratio between citric acid and metals was 6:1; the citric acid/ethylene glycol mass ratio was 60:40.

After partial evaporation of the water, the resin was heat treated at 300 °C for 2 h in a static oxidizing atmosphere which precipitated the partial decomposition of the polymeric gel (the expanded resin was constituted of partially pyrolyzed material). The product was removed from the beaker and milled. The powder was annealed at 400 °C (BMO-4 400 °C) and 700 °C (BMO-4 700 °C) for 2 h in a static oxidizing atmosphere at a heating rate of 10 °C/min.

### 2.3. Characterization of BaMoO<sub>4</sub> samples

The samples obtained were characterized by XRD using a Rigaku-DMax/2500PC (Japan) with Cu-K $\alpha$  radiation ( $\lambda=1.5406$  Å) in the  $2\theta$  range from 5° to 65° with a 0.02°/min increment. Lattice parameters and unit cell sample volumes were calculated using a least-square refinement REDE93 program. The average crystallite diameter (D<sub>crys</sub>) of the materials after heat treatment was determined by XRD results using the (112) diffraction peak of the BaMoO<sub>4</sub> phase where  $2\theta$  is located at around 26.5° according to the procedure described elsewhere [12]. The morphology and particle sizes of the as-prepared samples were observed using FE-SEM (Jeol JSM 6330F). The FT-IR spectrum was recorded with a Bruker Equinox-55 instrument. Infrared spectroscopy was used to monitor the bonding changes occurring during the synthesis process using the KBr pellet technique. Raman spectra were recorded on a RFS/100/S Bruker FT-Raman spectrometer, and a Nd:YAG laser provided an excitation light at 1064.0 nm with

a spectral resolution of  $4\text{ cm}^{-1}$ . PL data were recorded at room temperature using a U-1000 Jobin-Yvon double monochromator coupled with a cooled GaAs photomultiplier and a conventional photon counting system. The 350.7 nm exciting wavelength of an argon-ion laser was used; the laser maximum output power was maintained within 25 mW. All measurements were taken at room temperature.

### 3. Results and discussion

Table 1 lists methods used for the  $\text{BaMoO}_4$  synthesis. In the Czocharalski study [10], the spontaneous crystallization method [11] and the calcinations method by Hitoki [13], high temperatures and long time periods were required for the production of this material. Hasan [14] performed the calcination at a lower temperature (above  $450\text{ }^\circ\text{C}$ ), but the product of the reaction contains an additional phase ( $\text{BaO}_2 \cdot 8\text{H}_2\text{O}$ ). In the method used by Nassif [18], the temperature is above  $600\text{ }^\circ\text{C}$ ; however, the reaction time is long. Cavalcante et al obtained a single phase of  $\text{BaMoO}_4$  using the domestic MAH method with a reaction time of 1 h and a treatment temperature of about  $140\text{ }^\circ\text{C}$  [19,20]. In this study, mild conditions were used for material preparation as compared to the literature: at  $400\text{ }^\circ\text{C}$  and  $700\text{ }^\circ\text{C}$  for 120 min using the CP method and at  $100\text{ }^\circ\text{C}$  for 16 min using the MAH method. Both the CP and MAH methods used in this study produce  $\text{BaMoO}_4$  powders at low temperatures and short reaction times which results in a synthesis process at low cost.

XRD patterns of products synthesized by the CP and MAH methods are shown in Fig. 1. All samples possess as scheelite-type crystalline structure without an additional phase or impurities. All peaks observed in Fig. 1 can be indexed to the tetragonal  $\text{BaMoO}_4$  phase which is in agreement with standard data from JCPDS card no. 29-0193 [21]. From the peak positions displayed in Fig. 1, lattice parameters and unit cell sample volumes were calculated using a least-square refinement REDE93 program, and the average sample crystallite diameter ( $D_{\text{crys}}$ ) was determined using the (112) diffraction peak ( $2\theta$  around  $26.6$ ) according to the Scherrer equation [13]:

$$B = \kappa \times \lambda / (D_{\text{crys}} \times \cos \theta), \quad (1)$$

where  $B$  is the full width at half maximum (FWHM),  $\kappa$  is a constant,  $\lambda$  is the wavelength of the Cu  $\text{K}\alpha$  radiation and  $\theta$  is the Bragg angle. Fig. 2 shows the unit cell volume, crystallite

size and calculated lattice parameters ( $a$  and  $c$ ). Table 2 lists volume cell values and lattice parameter values obtained in this study and a comparison with values reported in the literature and JCPDS card [10,18,20–22].

Fig. 2a exhibits lattice parameters of the BMO-1, BMO-2, BMO-3 and BMO-4400  $^\circ\text{C}$  reaction systems. The  $a$  and  $c$  lattice parameters for these  $\text{BaMoO}_4$  powders are also close to bulk material lattice parameters of JCPDS card ( $a=5.5802\text{ \AA}$  and  $c=12.821\text{ \AA}$ ) [21]. Small differences can be related to small lattice distortions caused by residual stresses induced from preparation conditions and processing times. For BMO-1, the absence of a capping reagent and hydrothermal conditions seems to invoke an increase in the  $a$  lattice parameter and a shortening of the  $c$  lattice parameter in comparison with parameters of JCPDS card [21]. BMO-2 and BMO-3 were synthesized using the MAH method and did not show large variations in lattice parameter values. There was less increase in the  $c$  lattice parameter which was closer to the JCPDS card value for the BMO-3 sample; PEG was used as a capping reagent. The CP method used to obtain BMO-4 ( $400\text{ }^\circ\text{C}$  and  $700\text{ }^\circ\text{C}$ ) produced samples with  $a$  and  $c$  lattice parameters closer to bulk material lattice parameters of the JCPDS card [21]. These observations demonstrate that the crystal can be anisotropically grown depending on the method employed.

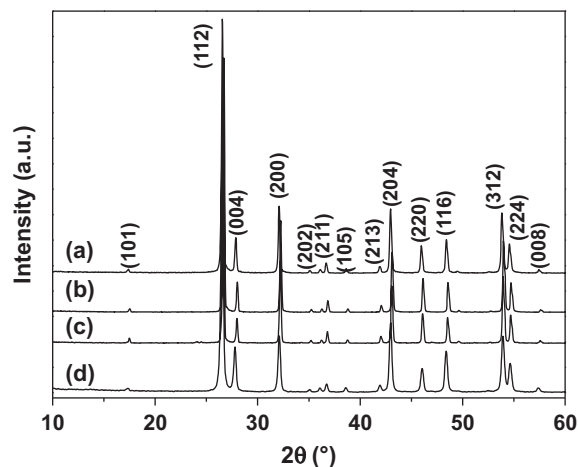


Fig. 1. XRD patterns of the BMO-1 (a), BMO-2 (b), BMO-3 (c) and BMO-4  $400\text{ }^\circ\text{C}$  (d).

Table 1  
Barium molybdate synthesis methods.

Method	T ( $^\circ\text{C}$ )	Time (h)	Morphology characteristics	Ba and Mo sources
Czocharalski [10]	1100–1200	30–40	bulk single crystals.	$\text{BaMoO}_4$
Spontaneous crystallization [11]	950	72	single crystals	$\text{BaMoO}_4$
Calcination [13]	900	24	—	$\text{BaMoO}_4$
Calcination [14]	450	3	—	$\text{BaMoO}_4$ , $\text{BaO}_2 \cdot 8\text{H}_2\text{O}$
$\text{BaCl}_2 + \text{Na}_2\text{MoO}_4$ [18]	600	72	—	$\text{BaMoO}_4$
DMH <sup>a</sup> [20]	140	1	octahedron-like	$\text{BaMoO}_4$
CP Method <sup>b</sup>	400	2	—	$\text{BaMoO}_4$
MAH <sup>b</sup>	100	0.27	octahedrons	$\text{BaMoO}_4$

<sup>a</sup>Domestic microwave-hydrothermal.

<sup>b</sup>This work.

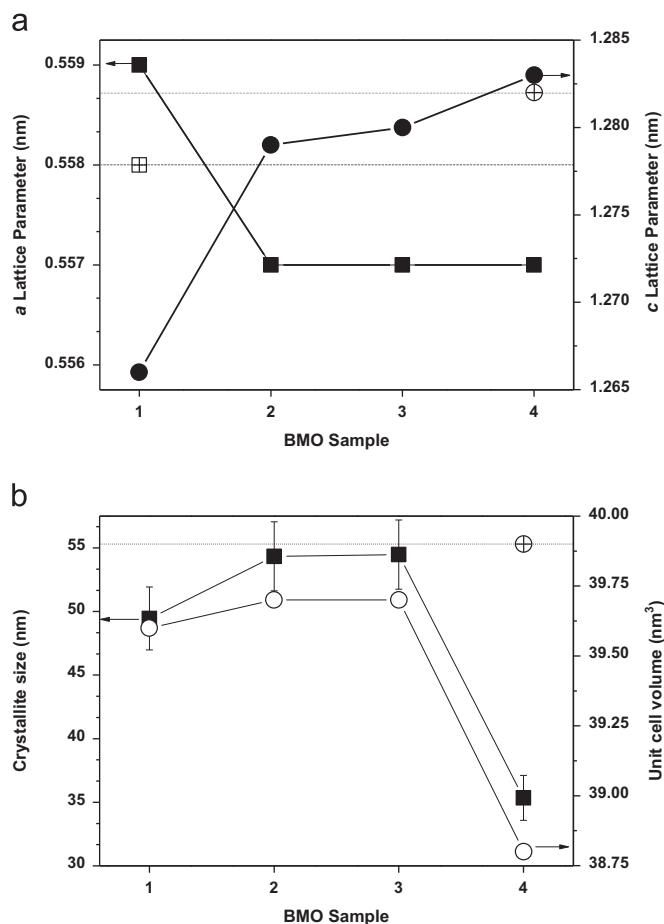


Fig. 2. Data obtained from the XRD patterns: Lattice parameters  $a$  (■) and  $c$  (●) of the BMO samples and of JCPDS card (⊕ and ⊕, respectively) (a); Crystallite size (■) and unit cell volume (●) values of BMO and JCPDS card (⊕) (b).

Table 2  
Lattice parameter and unit cell volume of BaMoO<sub>4</sub> powders.

Method	Lattice parameter (Å)		Unit cell volume (Å <sup>3</sup> )
	$a=b$	$c$	
Czocharalski [10]	5.62	12.82	405
BaCl <sub>2</sub> +Na <sub>2</sub> MoO <sub>4</sub> [18]	5.55	12.74	392
Domestic microwave-hydrothermal [20]	5.57	12.79	396
JCPDS card no. 29-0193 [21]	5.58	12.82	399
Complex polymerization method [22]	5.58	12.81	399
BMO-1 <sup>a</sup>	5.59	12.66	396
BMO-2 <sup>a</sup>	5.57	12.79	397
BMO-3 <sup>a</sup>	5.57	12.80	397
BMO-4 <sup>a</sup>	5.57	12.83	388

<sup>a</sup>This work.

The unit cell volume and crystallite size values of BMO are obtained from XRD data shown in Fig. 2b. The unit cell volumes were calculated from the product of the lattice parameters where in the scheelite crystalline structure type  $a=b$  and volume= $a \times a \times c$ . Unit cell volumes of BMO-2

and BMO-3 showed similar values (39.7 nm<sup>3</sup>); BMO-1 was slightly smaller (39.6 nm<sup>3</sup>); and BMO-4 was much smaller (38.8 nm<sup>3</sup>) in comparison to the unit cell volume value of the JCPDS card (39.9 nm<sup>3</sup>). BMO-4 exhibited less variation in the  $c$  lattice parameter and more variation in the  $a$  lattice parameter in comparison with the JCPDS card; however, the unit cell volume has a much lower value. Crystallite diameter ( $D_{\text{crys}}$ ) values of BaMoO<sub>4</sub> calculated by using Scherrer's equation were 49 nm ( $\pm 2$ ); 54 nm ( $\pm 3$ ); 54 nm ( $\pm 3$ ) and 44 nm ( $\pm 2$ ) for BMO-1, BMO-2, BMO-3 and BMO-4, respectively. The results followed the same trend of unit cell volume values and are very close to the results of Adhikari et al. [15] and Yoon et al. [16].

Well crystallized BaMoO<sub>4</sub> structures with predominantly octahedral morphologies are visible in FE-SEM micrographs (see Fig. 3(a–f)) for samples synthesized by the MAH method. BMO-4 samples (see Fig. 3(g–h)) synthesized by the CP method possess different morphologies for BMO-1, BMO-2 and BMO-3 samples that were obtained using the MAH method. This difference probably occurs because in the CP method the samples are derived from the pyrolysis of the resin (dry system) whereas in the MAH method it is mostly liquid. In the heterogeneous system with a major liquid phase, the crystalline unit can have freedom to grow in any direction (3D) while growth in solid systems is limited by particles that are in contact; therefore, in this case, differences among morphologies of BMO samples are expected.

FE-SEM images of BMO-2 and BMO-3 samples (see Fig. 3(c–f)) as compared with BMO-1 (see Fig. 3(a–b)) indicate that the higher pressure during the hydrothermal treatment produces modifications in the morphology. Fig. 3(c–d) shows superficial defects and distortions in micro-octahedra with a shortening of shapes. Fig. 3(e–f) confirms that a capping reagent associated with the MAH method can maintain octahedral morphology with aggregates of minor particles. BMO-3 micrographs suggest that the use of PEG as a capping reagent invokes the retention of morphology or the new formation of micro-octahedra. Therefore, processing conditions and the use of a capping reagent are imperative in the crystal growth process.

The average particle size distribution of BaMoO<sub>4</sub> samples was estimated by counting approximately 100 particles from FE-SEM micrographs. An average particle length distribution from 400 to 6400 nm (see Fig. 4(a)) was observed. It was verified that approximately 65% of the particles exhibit an average width between 900 and 1900 nm. After the MAH treatment, the average particle length showed a less dispersive distribution. Fig. 4(b, c) shows that 71% of the particles reached an average length between 750 and 1250 nm, and 69% of the particles exhibited an average length between 1500 and 2500 nm for BMO-2 and BMO-3, respectively.

The BMO-4 average particle length distribution shows results in the range 10 to 60 nm for BaMoO<sub>4</sub> powders heat treated at 400 °C and 300 to 1200 nm for powders treated at 700 °C (see Fig. 4(d, e)). It was verified that approximately 80% of the particles exhibit an average width of around 40 nm for the BMO-4 treated thermally at 400 °C (see Fig. 4(d)) and 61% between 450 and 650 nm for the BMO-4 treated

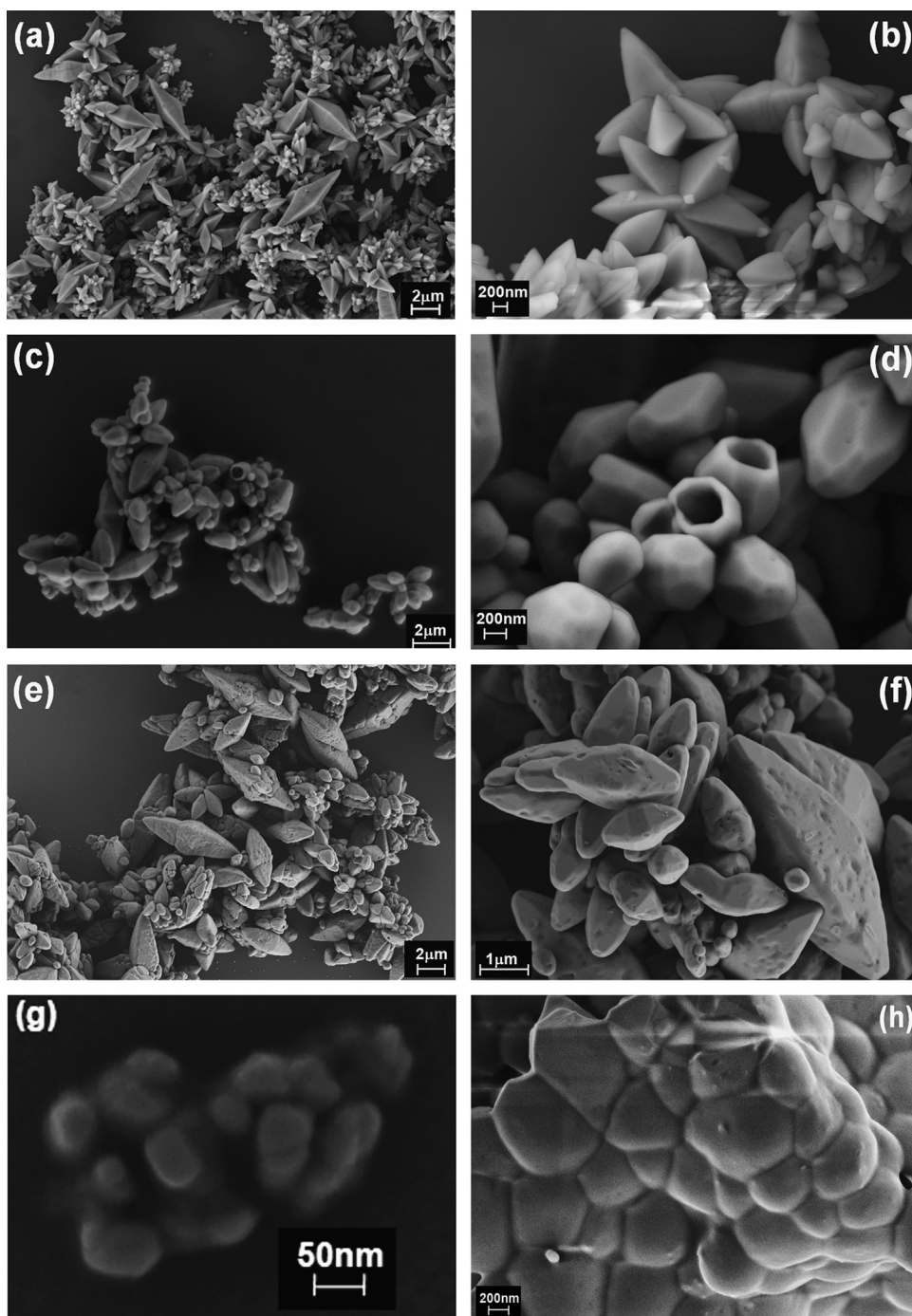


Fig. 3. FE-SEM images of the BMO-1 (a, b), BMO-2 (c, d), BMO-3 (e, f) and BMO-4 (g, h).

thermally at 700 °C (see Fig. 4(e)). FE-SEM images revealed that BMO-4 samples have an agglomerate of particles with an individual particle size of about 45 nm for samples treated at 400 °C (see Fig. 3(g)) and 600 nm for samples treated at 700 °C (see Fig. 3(h)). In the pyrolyzed resin of BMO-4, large numbers of small particles are in contact; this process of steps in the particle surface probably promotes the growth of grain contours which favor the sintering process and, consequently, the larger crystallite size [23]; therefore, it is appropriate to expect that the temperature increase in the heat treatment facilitates an increase in the size of the particle.

Sample Raman spectra are shown in Fig. 5, and the Raman mode frequencies are detailed in Table 3. Raman active mode peaks characteristic of BaMoO<sub>4</sub> scheelite structure are observed for all samples according to Basiev [10] where the BaMoO<sub>4</sub> primitive cell includes two internal and external groups. The [MoO<sub>4</sub>]<sup>2-</sup> ionic group with strong covalent Mo–O bonds is a peculiarity of the scheelite structure. Internal vibrations correspond to oscillations inside the [MoO<sub>4</sub>]<sup>2-</sup> molecular group with an immovable mass center. External or lattice phonons correspond to the Ba<sup>2+</sup> cation motion and the rigid molecular unit; only A<sub>g</sub>, B<sub>g</sub> and E<sub>g</sub> are Raman active

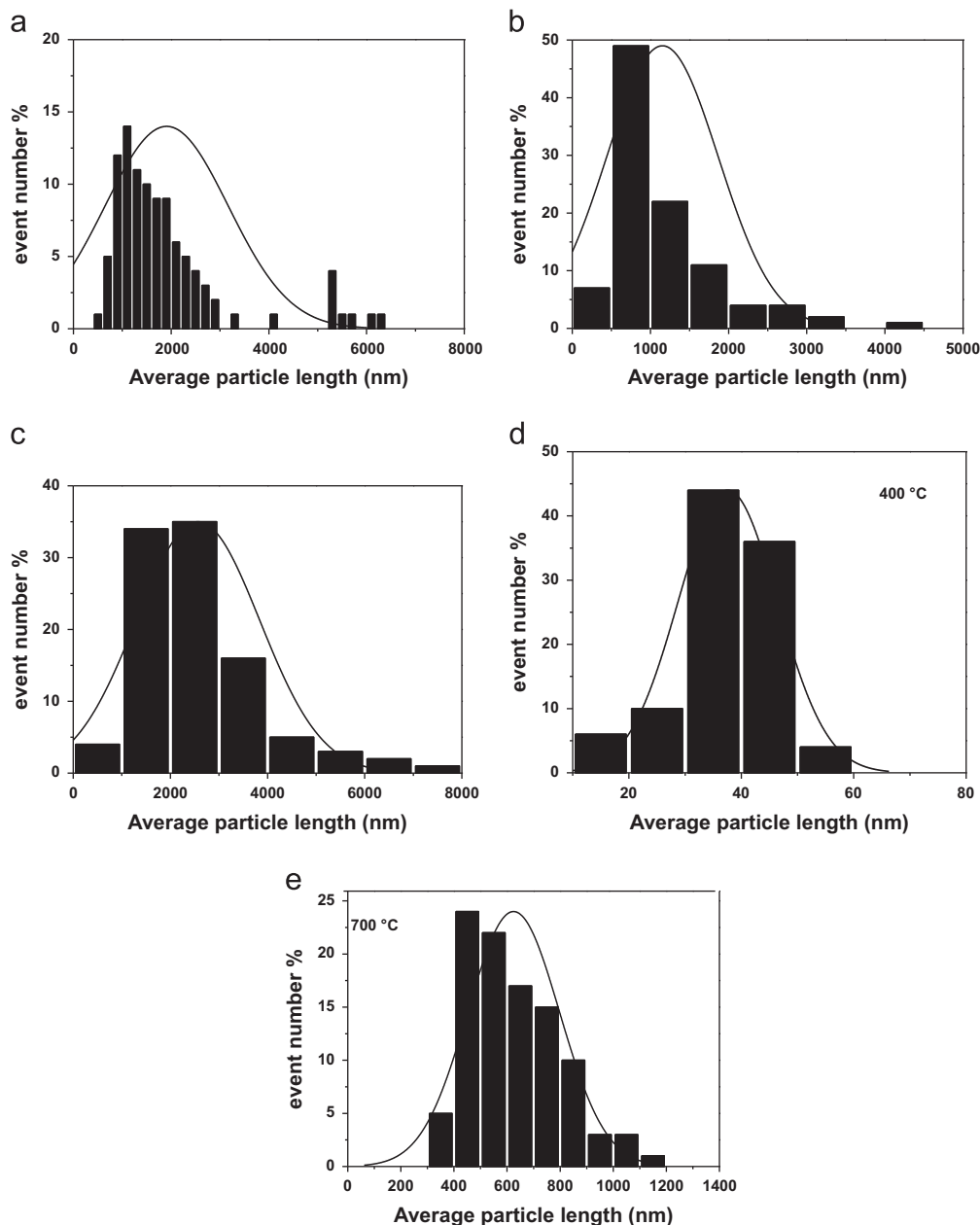


Fig. 4. Average particle length distributions of the BMO-1 (a), BMO-2 (b), BMO-3 (c), BMO-4 400 °C (d) and BMO-4 700 °C (e).

modes. The results display three sets of defined peaks between 70 and 190  $\text{cm}^{-1}$ , 300 and 400  $\text{cm}^{-1}$ , and 750 and 950  $\text{cm}^{-1}$ . The peaks correspond to  $\text{MoO}_2^{2-}$  external modes and  $\text{Ba}^{2+}$  motions and free rotation;  $\nu_2$  ( $E$ ) and  $\nu_4$  ( $F_2$ ); and  $\nu_3$  ( $F_2$ ) and  $\nu_1$  ( $A_1$ ) Raman modes, respectively. The BMO-2 sample obtained after the MAH treatment without a capping agent showed intense narrow defined peaks in the first, second and third sets which indicates a lower structural order-disorder ratio for both BMO-1 and BMO-3 samples according to PL results (see Fig. 6).

The Raman spectrum of the BMO-4 sample heat treated at 400 °C does not show well-resolved sharp peaks. The peaks correspond to external modes of  $\text{MoO}_2^{2-}$  and  $\text{Ba}^{2+}$  motions and free rotation; i.e.,  $\nu_2$  ( $E$ ) and  $\nu_4$  ( $F_2$ ) and  $\nu_3$  ( $F_2$ ) and  $\nu_1$  ( $A_1$ )

are absent, but crystallization was observed by XRD. This disagreement among XRD and Raman data probably occurs because materials are disordered at a middle distance with defects that are periodically repeated at long distance, which indicates that this material has a higher disorder at short- and intermediate-ranges in comparison with other samples [22]. Raman data for BMO-4 treated at 700 °C is similar to BMO-1, BMO-2 and BMO-3; defined peaks are visible in three regions of the spectrum: between 70 and 190  $\text{cm}^{-1}$ , 300 and 400  $\text{cm}^{-1}$ , and 750 and 950  $\text{cm}^{-1}$ . The  $[\text{MoO}_4]^{2-}$  molecular group observed in Raman data can be confirmed by FTIR spectra for all samples; these spectra showed the main absorption band in the region around 856  $\text{cm}^{-1}$  assigned to  $F_2(\nu_3)$  antisymmetric stretch vibrations which is associated

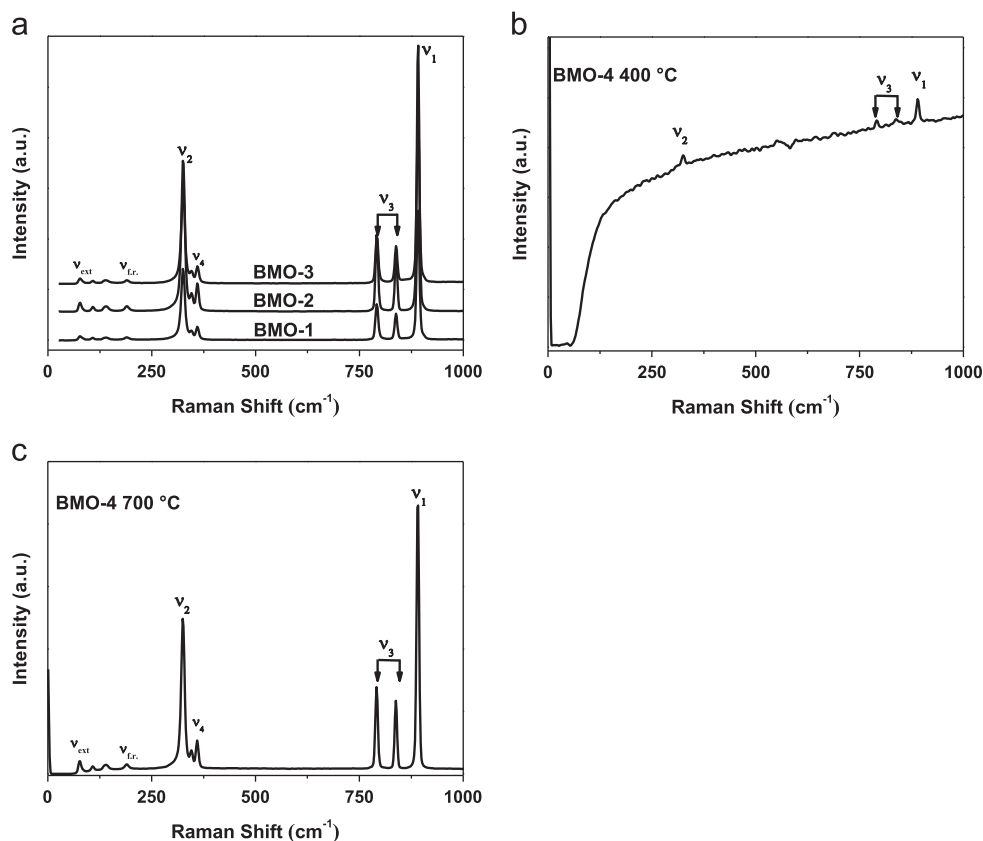


Fig. 5. Raman spectra of the BMO-1, BMO-2 BMO-3 (a), BMO-4 400 °C (b) and BMO-4 700 °C (c).

Table 3  
Raman mode frequencies in BaMoO<sub>4</sub> powders prepared at different temperatures.

Lattice mode symmetry $C_{4h}^6$	BaMoO <sub>4</sub>						Assignments
	BMO-1	BMO-2	BMO-3	BMO-4400 °C	BMO-4700 °C	1100–1200 °C <sup>a</sup>	
$A_g$	892		892	890	892	892	$\nu_1$ ( $A_1$ )
$B_g$	838	892	838	838	838	837	$\nu_3$ ( $F_2$ )
$E_g$	792	838	791	791	791	791	
$E_g$	359	791	359		359	358	$\nu_4$ ( $F_2$ )
$B_g$	346	359	346		346	345	
$B_g$	327	346	327		327	324	$\nu_2$ ( $E$ )
$A_g$	325	327	325	325	325	324	
$E_g$	190	325	190		190	188	$\nu_{fr.}$ ( $F_1$ ) free rotation
$B_g$	139	191	139		139	137	$\nu_{ext.}$ – external Modes MoO <sub>4</sub> <sup>2-</sup> and Ba <sup>2+</sup> motions
$E_g$	108	140	109		109	110	
$B_g$	77	108	76		76	76	
$E_g$		77				74	

<sup>a</sup>Czocharalski [10].

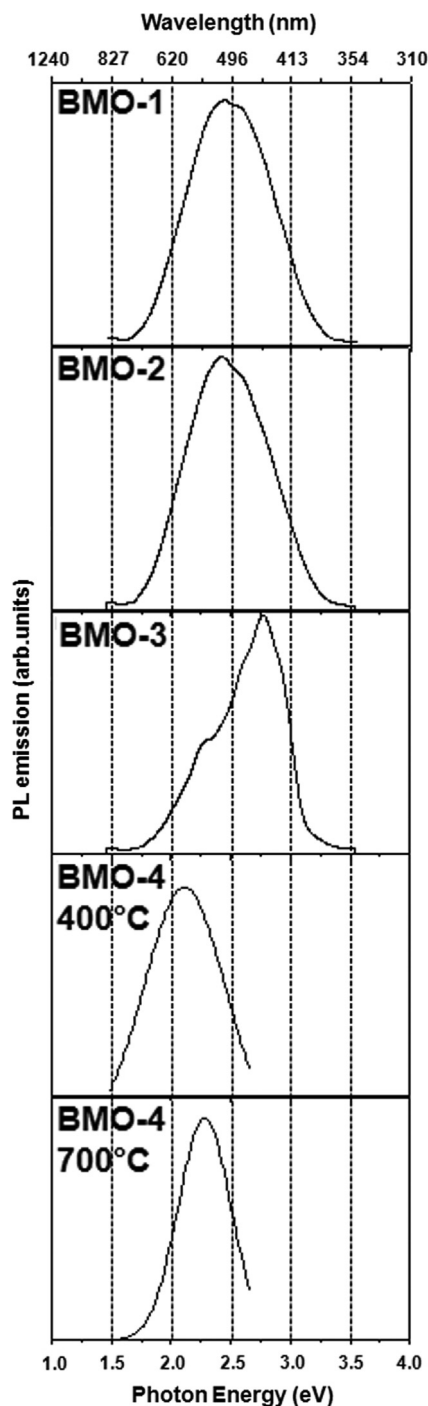


Fig. 6. PL spectra of the BaMoO<sub>4</sub> samples.

with the Mo–O stretching vibration in a MoO<sub>4</sub><sup>2-</sup> tetrahedron. FTIR spectra showed that all samples are free of residual organic groups [22,24].

BMO-1, BMO-2, BMO-3 and BMO-4 samples were crystalline and showed scheelite-type phases by DRX, Raman and FTIR data. Nevertheless, one disorder degree at short- and intermediate-ranges in the crystalline structure of the BMO-4 sample heat treated at 400 °C was observed by Raman spectroscopy which is an effective tool for studying the structural order and disorder. For a perfect crystal, the first-

order Raman phonon spectrum consists of narrow lines that correspond to Raman-allowed zone center (*Γ*-point) modes definite polarization selection rules. However, for disordered crystals, the following features are anticipated in the phonon spectrum: (1) a broadening of the first-order Raman lines; (2) the activation of forbidden Raman phonons; (3) the appearance of broad Raman bands reflecting the phonon density of states; (4) frequency shifting of some peaks proportional to the dopant element concentration (i.e., one-phonon-like behavior); and (5) the splitting of a number peaks involving different elements that share the same lattice site (i.e., two-phonon-like behavior) [25,26]. For ordered crystals analyzed by Raman spectrum with characteristic narrow lines, the maximum FWHM values from Bragg reflections and Raman bands were calculated and are listed in Table 4. These observations demonstrate that these materials have different levels of deep defects which depend upon thermal treatment and the addition of a capping reagent. If narrow lines are characteristics of an ordered crystal, as discussed previously, then BMO-4 treated at 400 °C has more disordered material, and BMO-2 has more structurally ordered material which agrees with FE-SEM micrograph interpretations (see Fig. 3). However, these characterization techniques did not facilitate a study of material energy levels.

More ordered structures are expected to have a higher gap energy than structures less ordered because defects promote intermediate stages between acceptor and donor bands which decreases gap energy values [26]. According to this theory, gap data calculated for BMO-2 (material is more ordered) and BMO-4 heat treated at 400 °C (material is more disordered), were 4.35 and 3.85 eV for BMO-2 and BMO-4 samples, respectively. The PL spectrum is also a powerful tool for providing important information about the physical properties of materials at the molecular level, including shallow and deep level defects. PL emission of the molybdate group originates from intrinsic defects; higher-ordered and higher-defect density structures (amorphous materials) are unfavorable conditions for intense PL emission [22].

Fig. 6 illustrates PL spectra obtained at room temperature for BaMoO<sub>4</sub> crystals in this study. PL spectra exhibit a broad band covering the visible electromagnetic region from 400 to 700 nm which is typical of a multi-phonon and multi-level process; i.e., a system in which relaxation occurs by several paths involving the participation of numerous states within the material band gap. PL

Table 4

Full width at half maximum (FWHM) obtained through Raman and XRD data of the BMO powders.

Sample	Full Width at Half Maximum (FWHM)					
	Raman peak (cm <sup>-1</sup> )			XRD diffraction peak 2θ (°)		
	892	792	325	26.6	27.9	32.2
BMO-1(RT)	8.3	7.8	10.7	0.19	0.21	0.20
BMO-2(100 °C)	7.4	7.1	9.9	0.18	0.17	0.18
BMO-3(100 °C/peg)	8.3	7.8	10.7	0.18	0.18	0.19
BMO-4 (400 °C)	–	–	–	0.27	0.26	0.27
BMO-4 (700 °C)	6.9	7.1	9.2	0.20	0.20	0.22

curves of BMO-1 have a maximum at 508 nm (2.44 eV) and BMO-2 at 512 nm (2.42 eV). Both BMO-1 and BMO-2 samples presented a broad band with a predominance of green PL emission ( $\sim 510$  nm; 2.43 eV); the BMO-3 sample shows a band maximum dislocated to the blue emission at 447 nm (2.77 eV) which is the region of more optical transition energy. BMO-4 samples treated at 400 °C and 700 °C also present a broad band but with a predominance of orange PL emission. PL curves for BMO-4 heat treated at 400 °C and 700 °C have a maximum at 588 nm (2.11 eV) and 541 nm (2.29 eV), respectively.

These results indicate that the BMO-3 structure became more ordered with MAH treatment and the addition of a capping agent which favors the blue light emission (smaller wavelength) with higher energies. The PL BMO-3 profile indicates a considerable increase in energy states related to shallow holes due to the high band intensity located at around 447 nm (blue emission). The opposite is observed for BMO-4 treated at 400 °C and obtained by the CP method. This synthesis process favors the structural disorder of material

which creates intermediary levels in the gap band that facilitate the multi-phonon transition process; consequently, PL emission can occur in lower energy regions or in the orange region. The emission energy increase is linked to the structural order increase and is associated with shallow defects and disorder which is linked to deep defects inserted in the band-gap.

To gain a better understanding of PL properties and their dependence on the lattice structural order-disorder, PL curves were analyzed using the PeakFit deconvolution program [27]. Assuming PL emission peaks can be described with a Gaussian function, the emission envelope in Fig. 6 can be fitted by multiple peaks and analyzed. Fig. 7 illustrates this decomposition and the areas under the curve of the respective transitions.

BaMoO<sub>4</sub> PL curves for all samples are composed of five PL components: blue (maximum in 428 nm), blue–green (maximum in 459 nm), green (maximum in 509 nm), yellow (maximum in 557 nm), orange (maximum in 614 nm), orange–red (maximum in 686 nm) and red (maximum in 726 nm) which refer to the region where the component maximum appears. Each color represents a

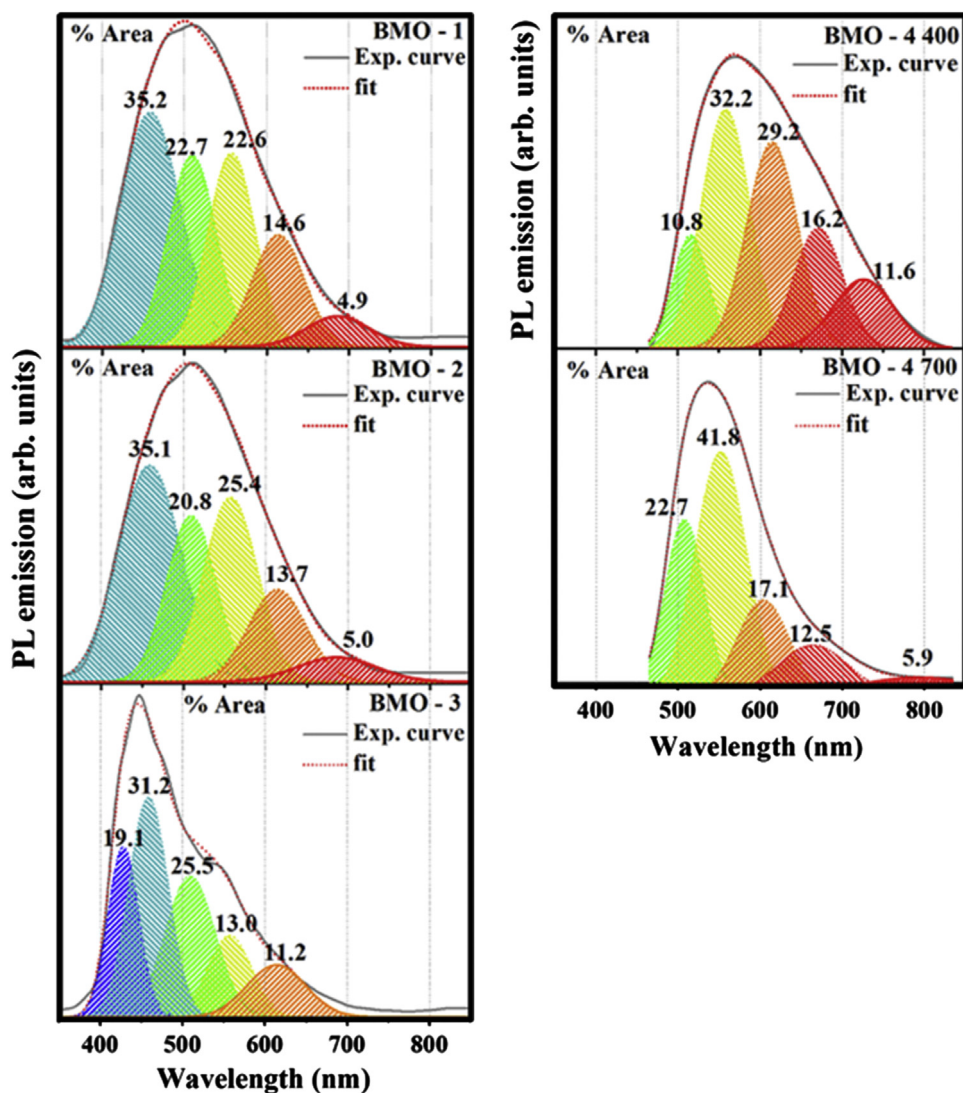


Fig. 7. Deconvolution of PL curves fitted for the BMO samples and area percentage of fitting parameters.

different type of electronic transition and is linked to a specific structural arrangement. In PL spectra of a more ordered structure, areas designated as yellow, orange and red decrease while the areas designated as green and blue increase. A yellow–orange–red emission is linked to a disordered structure with deep defects, and a blue–green emission is linked to an ordered structure with shallow defects [28].

Two effects in the PL emission of the BMO samples can be identified. The first effect is a consequence of structural factors in the scheelite as the intrinsic distortion, asymmetric distortion [MoO<sub>4</sub>] tetrahedra and [BaO<sub>8</sub>] octahedra [2]. The asymmetric distortion allows the self-trapping of electrons and holes during radioactive decay. The second effect is a result of the surface defect that modifies PL emissions. Other factors can also influence PL properties regarding the degree of aggregation and alignment between particles, and surface defects.

Surface defect states and interfaces populate additional levels in the band gap of the material that facilitates a decrease in the band gap. If the surface state is controlled, the particle size and morphology can be restricted, deep and shallow defects can be controlled and PL properties can be modified accordingly.

#### 4. Conclusions

In summary, barium molybdate particles (BaMoO<sub>4</sub>) were prepared by two routes (MAH and CP methods) with variations in applied experimental parameters. Scheelite-type single crystalline structures of BaMoO<sub>4</sub> were identified by XRD, Raman and FTIR. Octahedral morphologies were characterized by microscopy FE-SEM. The influence of the synthesis method on the morphology, particle size, dispersion uniformity and on the optical properties of BaMoO<sub>4</sub> was observed through the use of two different synthesis methods and a capping reagent. PL properties of samples indicate there is a relationship with the electronic order-disorder at short and intermediate material ranges and shallow and deep defects in the structure surface with interfaces that populate additional levels in the band gap and consequently, with the utilized synthesis method. If the particle size and morphology are controlled, deep and shallow defects will be controlled, and PL properties will be modified as desired.

#### Acknowledgement

The authors acknowledge the support of Brazilian agencies CNPq, FAPESP-CEPID and CAPES. This work was partially supported by CNPq, under Process #576563/2008-0.

#### References

- [1] R.C. Lima, L.R. Macario, J.W.M. Espinosa, V.M. Longo, R. Erlo, N.L. Marana, J.R. Sambrano, M.L.D. Santos, A.P. Moura, P.S. Pizani, J. Andr es, E. Longo, J.A. Varela, Toward an understanding of intermediate- and short-range defects in ZnO single crystals. A combined experimental and theoretical study, *J. Phys. Chem. A* 112 (38) (2008) 8970–8978.
- [2] V.M. Longo, A.T. de Figueiredo, S. de Lazaro, M.F. Gurgel, M.G. S. Costa, C.O. Paiva-Santos, J.A. Varela, E. Longo, V.R. Mastelaro, F.S. De Vicente, A.C. Hernandez, R.W.A. Franco, Structural conditions that leads to photoluminescence emission in SrTiO<sub>3</sub>: an experimental and theoretical approach, *J. Appl. Phys.* 104 (2) (2008) 02351–02362.
- [3] N. Klassen, S. Shmurak, B. Red'kin, B. Ille, M. Lebeau, P. Lecoq, M. Schneegans, Correlations between structural and scintillation characteristics of lead and cadmium tungstates, *Nucl. Instrum. Methods Phys. Res. Sect. A – Accel. Spectrom. Detect. Assoc. Equip.* 486 (1–2) (2002) 431–436.
- [4] Y. Sun, J. Ma, J. Fang, C. Gao, Z. Liu, Synthesis of BaMoO<sub>4</sub> high photoluminescent whiskers by an electrochemical method, *Ceram. Int.* 37 (2) (2011) 683–686.
- [5] C.S. Riccardi, R.C. Lima, M.L.D. Santos, P.R. Bueno, J.A. Varela, E. Longo, Preparation of CeO<sub>2</sub> by a simple microwave-hydrothermal method, *Solid State Ionics* 180 (2–3) (2009) 288–291.
- [6] J. Kubo, W. Ueda, Catalytic behavior of AMoO(x) (A=Ba, Sr) in oxidation of 2-propanol, *Mater. Res. Bull.* 44 (4) (2008) 906–912.
- [7] J.H. Ryu, J. Yoon, C.S. Lim, K.B. Shim, Microwave-assisted synthesis of barium molybdate by a citrate complex method and oriented aggregation, *Mater. Res. Bull.* 40 (9) (2005) 1468–1476.
- [8] F.A. Kroger, *Some Aspects of the Luminescence of Sol*, Elsevier, Amsterdam, 1948.
- [9] C. Pupp, R. Yamdagni, R.F. Porter, Mass spectrometric study of evaporation of BaMoO<sub>4</sub> and BaWO<sub>4</sub>, *J. Inorg. Nucl. Chem.* 31 (7) (1969) 2021–2029.
- [10] T.T. Basiev, A.A. Sobol, Y.K. Voronko, P.G. Zverev, Spontaneous Raman spectroscopy of tungstate and molybdate crystals for Raman lasers, *Opt. Mater.* 15 (3) (2000) 205–216.
- [11] D.A. Spassky, S.N. Ivanov, V.N. Kolobanov, V.V. Mikhailin, V.N. Zemskov, B.I. Zadneprovski, L.I. Potkin, Optical and luminescent properties of the lead and barium molybdates, *Radiat. Meas.* 38 (4–6) (2004) 607–610.
- [12] A.P.A. Marques, F.C. Picon, D.M.A. Melo, P.S. Pizani, E.R. Leite, J. A. Varela, E. Longo, Effect of the order and disorder of BaMoO<sub>4</sub> powders in photoluminescent properties, *J. Fluoresc.* 18 (1) (2008) 51–59.
- [13] G. Hitoki, T. Takata, S. Ikeda, M. Hara, J.N. Kondo, M. Kakihana, K. Domen, Mechano-catalytic overall water splitting on some mixed oxides, *Catal. Today* 63 (2–4) (2000) 175–181.
- [14] M.A. Hasan, M.I. Zaki, K. Kumari, L. Pasupulety, Soot deep oxidation catalyzed by molybdena and molybdates: a thermogravimetric investigation, *Thermochim. Acta* 320 (1–2) (1998) 23–32.
- [15] R. Adhikari, G. Gyawali, T.H. Kim, T. Sekino, S.W. Lee, Synthesis of Er<sup>3+</sup> loaded barium molybdate nanoparticles: a new approach for harvesting solar energy, *Mater. Lett.* 91 (2013) 294–297.
- [16] J.W. Yoon, J.H. Ryu, K.B. Shim, Photoluminescence in nanocrystalline MMoO<sub>4</sub> (M=Ca, Ba) synthesized by a polymerized complex method, *Mater. Sci. Eng. B-Solid State Mater. Adv. Technol.* 127 (2–3) (2006) 154–158.
- [17] Z. Luo, H. Li, H. Shu, K. Wang, J.X. Xia, Y.S. Yan, Synthesis of BaMoO<sub>4</sub> nestlike nanostructures under a new growth mechanism, *Cryst. Growth Des.* 8 (7) (2008) 2275–2281.
- [18] V. Nassif, R.E. Carbonio, Neutron diffraction study of the crystal structure of BaMoO<sub>4</sub>: a suitable precursor for metallic BaMoO<sub>3</sub> perovskite, *J. Solid State Chem.* 146 (1) (1999) 266–270.
- [19] L.S. Cavalcante, J.C. Sczancoski, R.L. Tranquilin, J.A. Varela, E. Longo, M.O. Orlandi, Growth mechanism of octahedron-like BaMoO<sub>4</sub> microcrystals processed in microwave-hydrothermal: Experimental observations and computational modeling, *Particuology* 7 (5) (2009) 353–362.
- [20] L.S. Cavalcante, J.C. Sczancoski, R.L. Tranquilin, M.R. Joya, P. S. Pizani, J.A. Varela, E. Longo, BaMoO<sub>4</sub> powders processed in domestic microwave-hydrothermal: synthesis, characterization and photoluminescence at room temperature, *J. Phys. Chem. Solids* 69 (11) (2008) 2674–2680.
- [21] JCPDS card no. 29-0193.
- [22] A.P.A. Marques, D.M.A. de Melo, C.A. Paskocimas, P.S. Pizani, M.R. Joya, E.R. Leite, E. Longo, Photoluminescent BaMoO<sub>4</sub> nanopowders prepared by complex polymerization method (CPM), *J. Solid State Chem.* 179 (2006) 658–665.

- [23] W.D. Kingery, *Ceramic Fabrication Processes*, MIT Press, Cambridge, 1957.
- [24] K. Nakamoto, *Infrared and Raman Spectra of Inorganic and Coordination Compounds*, Wiley, New York, 1986.
- [25] M.R. Moura, A.P. Ayala, I. Guedes, M. Grimsditch, C.K. Loong, L.A. Boatner, Raman scattering study of  $\text{Tb}(\text{V}_{1-x}\text{P}_x)\text{O}^{-4}$  single crystals, *J. Appl. Phys.* 95 (3) (2004) 1148–1151.
- [26] A.P.A. Marques, F.V. Motta, D.M. Melo, P.S. Pizani, E.R. Leite, J.A. Varela, E. Longo, Evolution of photoluminescence as a function of the structural order or disorder in  $\text{CaMoO}_4$  nanopowders, *J. Appl. Phys.* 104 (4) (2008) 043505 (–1).
- [27] T. Ding, W.T. Zheng, H.W. Tian, J.F. Zang, Z.D. Zhao, S.S. Yu, X.T. Li, F.L. Meng, Y.M. Wang, X.G. Kong, Temperature-dependent photoluminescence in  $\text{La}_{2/3}\text{Ca}_{1/3}\text{MnO}_3$ , *Solid State Commun.* 132 (12) (2004) 815–819.
- [28] V.M. Longo, E. Orhan, L.S. Cavalcante, S.L. Porto, J.W.M. Espinosa, J.A. Varela, E. Longo, Understanding the origin of photoluminescence in disordered  $\text{Ca}_{0.60}\text{Sr}_{0.40}\text{WO}_4$ : An experimental and first-principles study, *Chem. Phys.* 334 (1–3) (2007) 180–188.